Original Research Article

SHM Structural Health Monitoring

Structural Health Monitoring
1–25

DOI: 10.1177/14759217261422513
journals.sagepub.com/home/shm
Sage

Unified health domain relation learning for train transmission systems fault detection under varying operating conditions

Zuoyi Chen[1,2*], Zhixu Duan[1*], Hua-Ming Qian[1,2] and Hong-Zhong Huang[1,2]

Abstract

Reliable fault detection in train transmission systems is essential for safe and efficient railway operation, yet it is challenged by variable operating conditions and scarce fault samples. To address these issues, a novel unified health domain relation learning (UHDRL) framework is proposed. Specifically, a pseudofault sample library is constructed to generate diverse synthetic fault examples, reducing UHDRL's reliance on healthy samples. A unified health domain mechanism is designed to map the different operating conditions into a common feature space, thereby reducing distribution shifts caused by operating variations. Additionally, a health relation learning mechanism is proposed to construct feature pairs between healthy representations and pseudo-faults to uncover intrinsic and discriminative attributes of health states. Experiments on three train transmission systems, conducted under both deterministic and non-deterministic operating condition changes, demonstrate that UHDRL is highly adaptable and robust in zero-fault-sample settings, improving detection accuracy by over 12% compared with existing methods.

Keywords

Train transmission systems, fault detection, zero-faulty samples, varying operating conditions, relation network

Introduction

The reliability of train transmission systems (TTS) is vital for the safety and efficiency of railway networks. These systems operate under varying operating conditions, including fluctuating speeds, load variations, temperature extremes, and wear, which contribute to component degradation and increase the risk of failures.[1–4] Timely and accurate fault detection is essential for predictive maintenance and smooth operations.[5–7] Machine learning and deep learning (DL) approaches have recently shown promising results for train transmission systems fault detection by analyzing monitoring data.[8–11] Nevertheless, such methods typically require large labeled fault datasets and assume that training and test distributions match.[12–15] In practice, fault samples are often scarce or absent, and distribution shifts induced by varying operating conditions, environmental factors, or train configurations undermine model generalization and increase misclassification rates under unseen conditions.

Transfer learning (TL) has been widely explored to mitigate these issues by transferring diagnostic knowledge from a source condition to a target condition via domain adaptation techniques.[16–18] While TL reduces dependence on labeled target data, it still relies on fault samples from source domains and its success depends strongly on the similarity between source and target distributions.[19–21] In train transmissions, substantial heterogeneity across train types, operating regimes, and environments often leads to distributional discrepancies that hinder effective knowledge transfer. Moreover, identifying suitable source domains and coping with complex interactions among operating

[1]School of Mechanical and Electrical Engineering, University of Electronic Science and Technology of China, Chengdu, China
[2]Center for System Reliability and Safety, University of Electronic Science and Technology of China, Chengdu, China

*These authors contributed equally to this work, they are co-first authors of the article.

Corresponding author:
Zuoyi Chen, School of Mechanical and Electrical Engineering, University of Electronic Science and Technology of China, Chengdu 611731, China.
Email: zuoyichen@uestc.edu.cn

factors increase the difficulty and computational cost of deploying TL in diverse real-world settings.

Prior work has therefore focused on disentangling health-state representations from operating parameters to improve robustness. For instance, Sun et al.[22] employed contrastive learning methods to explore the representation of health samples across varying environments. Zhou et al.[23] proposed a conditional variational autoencoder to separate operating conditions from health state, extracting statistical features from the reduced-dimensional latent variables as fault indicators. Hu et al.[24] examined the causal relationships between observed signals, operating conditions, and health state, developing a decoupling objective grounded in mutual information theory, and using variational inference and self-supervised learning to extract abnormal indicators independent of operating conditions for fault detection. Wu et al.[25] introduced a domain-adversarial regression strategy to steer the training of decoupled autoencoders under changing operating conditions.

Although these methods improve robustness to some operating variations, they have notable limitations. First, they rely heavily on healthy-state samples and thus are overly sensitive to changes in operating conditions. In train systems, the same condition can exhibit markedly different features under high versus low speed or full versus light load, and a single training set rarely captures this variability, which leads to overfitting and degraded real-world detection performance. Second, many approaches assume deterministic variations and neglect complex interactions among temperature, terrain, and track conditions. Real-world operating environments are more dynamic and uncertain, and the distributions of faulty and healthy states may differ substantially across conditions. As a result, methods that depend mainly on healthy samples struggle to establish clear decision boundaries, causing overlap between healthy and faulty classes, limiting cross-condition generalization, and increasing false alarm rates.

To address the fault detection challenges in train transmission systems under zero-fault samples and varying operating conditions, an innovative unified health domain relation learning (UHDRL) framework is proposed. The proposed UHDRL framework incorporates several key components. First, a pseudo-fault sample library (PFSL) is established to increase the diversity of training samples, reducing the UHDRL's over-sensitivity to health state and markedly improving its ability to detect fault state. Second, a unified health domain mechanism (UHDM) is designed to map health samples from diverse operating conditions into a unified feature space, effectively minimizing the disruption caused by fluctuations in operating conditions to the consistency of the health sample distribution. Building on this, a health relation learning mechanism (HRLM) is proposed, which creates feature pairs by combining health features from different operating conditions with PFSL, facilitating a deeper extraction of the intrinsic features of the health state. Finally, by forming feature pairs between target and health samples and assessing their similarity, the system accurately determines the state types of the train transmission system.

The primary contributions of this article are (1) The UHDRL is proposed to address the challenge of accurately detecting faults in train transmission system under varying operating conditions and zero-faulty samples. Experimental results demonstrate its effectiveness in detecting faults across three high-speed train transmission systems, achieving over 12% improvement in detection accuracy compared to existing methods. (2) The UHDM is designed to integrate health samples from different operating conditions into a shared boundary space. By minimizing the distribution differences caused by operating condition variations, it establishes consistent detection boundaries, significantly enhancing the UHDRL's adaptability under diverse conditions. (3) An innovative feature concatenation mechanism in HRLM is designed, which constructs feature pairs between health state samples and PFSL under different operating conditions, revealing the unique and inherent attributes of the health state. This mechanism greatly enhances the precision of fault identification in the UHDRL by refining its capability to detect minor variations between fault and health states.

The article is structured in the following manner. Section "Methodology" offers a detailed explanation of methodology. Section "The fault detection framework base on UHDRL" outlines the fault detection framework. Section "Case study" includes a thorough assessment of the experimental outcomes, and Section "Conclusion" wraps up the research with concluding remarks.

Methodology

UHDRL structure

Figure 1 illustrates the UHDRL structure, which primarily consists of the PFSL, feature extractor, the UHDM, and the HRLM.

Assume that the train transmission system operates under n distinct operating conditions, with health state samples $D_H(D_H^1, \cdots, D_H^n)$ representing the health states across these conditions C_i, where D_H^n corresponds to the health state sample for the operating condition C_n. When fault samples are unavailable, constructing a

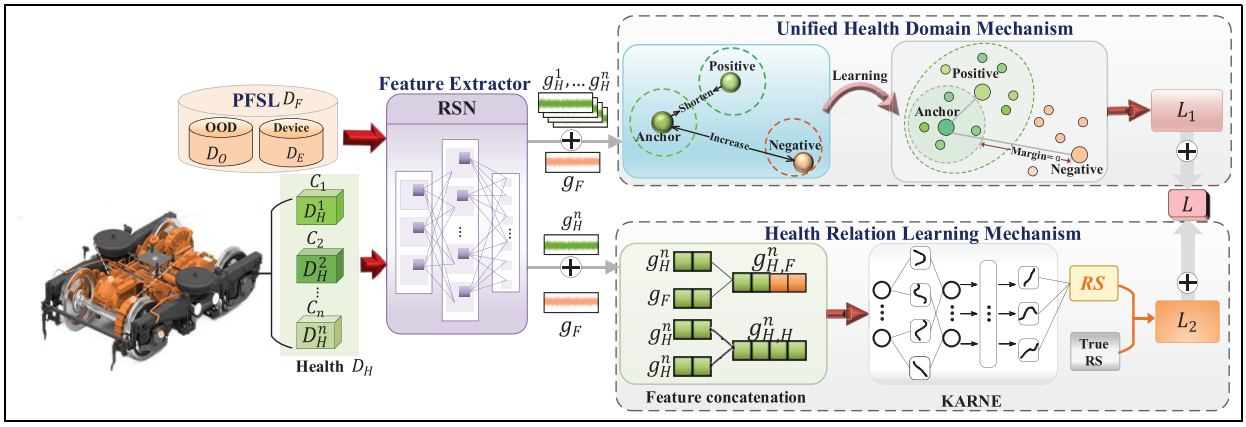

Figure 1. UHDRL structure.
UHDRL: Unified health domain relation learning.

fault detection model solely using health state samples may result in over-sensitivity to variations in health states. In the context of train transmission systems, health states can differ significantly across different operating conditions, and relying directly on health state samples may fail to capture the true characteristics of faults. To enhance the robustness of the fault detection model, a PFSL D_F is constructed, incorporating out-of-distribution samples and fault samples from other devices. This broadens the diversity of the samples and strengthens the model's fault detection capability. The health state samples D_H and PFSL D_F are then input into the feature extractor, which extracts corresponding health state features $g_H(g_H^1, g_H^2, \cdots, g_H^n)$ PFSL features g_F.

To effectively mitigate the impact of fluctuations in operating conditions on the sample distribution of health state, the UHDM is designed to consolidate all health samples from different operating conditions within a unified spatial boundary. As illustrated in Figure 1, the anchor-based alignment strategy begins by randomly selecting a health feature from one operating condition as the anchor point. Next, a health feature from different operating condition is chosen as the positive sample, while the PFSL serves as the negative sample. The positive sample is drawn toward the anchor point, whereas the negative sample is repelled, creating a boundary reconstruction loss, denoted as L_1. This process ensures that health state features from different conditions are unified in the same spatial boundary, while PFSL is excluded from this boundary, effectively eliminating the distribution differences caused by fluctuations in operating conditions.

In the absence of fault samples and amidst fluctuations in operating conditions, extracting the intrinsic features of health states across diverse conditions becomes particularly critical. To address this, the HRLM is designed to connect the health state features from different operating conditions with those from the PFSL, forming feature pairs that reveal the intrinsic attributes of health states. This mechanism's innovation lies in its ability to concatenate feature pairs from different state types, enabling the HRLM to effectively capture the core features of health states under varying operating conditions, rather than depending on health samples from specific conditions. These concatenated feature pairs are input into Kolmogorov–Arnold network relation evaluator (KANRE) to uncover the underlying relationships between the health state and PFSL features. The KANRE computes the corresponding relation scores, forming a loss function L_2. Ultimately, by combining the losses L_1 and L_2, the total loss function L is formed, which is iteratively optimized to improve the UHDRL's fault detection accuracy and robustness under varying operating conditions.

PFSL construction

As depicted in Figure 2, the PFSL D_F is constructed by integrating two distinct data sources: external equipment fault samples D_E and generated out-of-distribution samples $D_O(D_O^1, D_O^2, \cdots, D_O^n)$. The external equipment fault samples D_E are compiled by transferring historical fault data from similar devices (e.g., gearboxes of different models). These samples encompass common fault modes in transmission systems, such as gear breakage and bearing wear. While device-to-device physical differences exist, D_E serves to provide the model with diverse, generic fault patterns that act as broad "negative" constraints.

To explicitly address the device-specific characteristics and bridge potential domain gaps caused by external data, the out-of-distribution samples D_O are generated based on health state samples D_H^i from

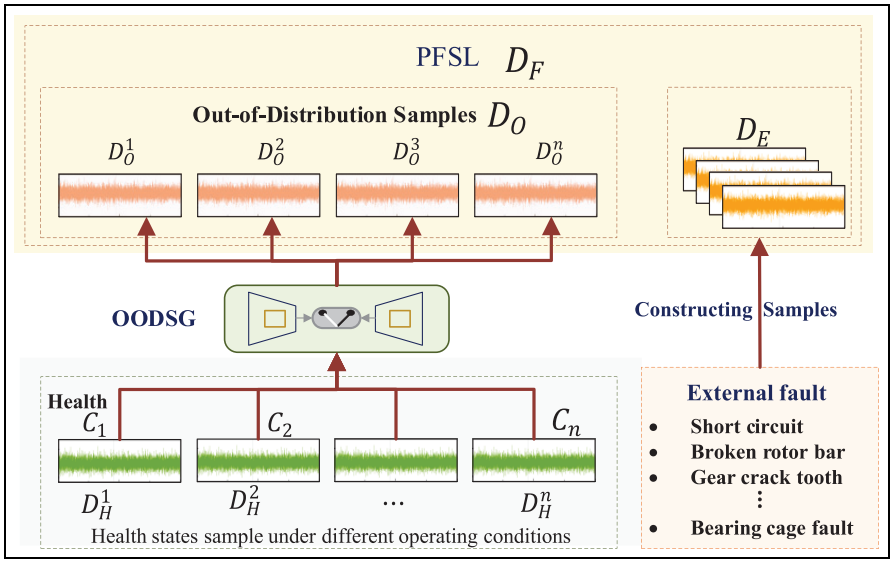

Figure 2. PFSL construction.
PFSL: Pseudo-fault sample library.

different operating conditions C_i. Specifically, for each operating condition C_i, multiple out-of-distribution samples D_O^i are synthesized from the corresponding health samples D_H^i using the modified Soft Brownian Offset method.[26] This ensures that the generated pseudofaults are tailored to the specific feature distribution of the target device. The generation mechanism is outlined as follows:

$$D_O^i = G\left(D_H^i, N\right) = \sum_{j=1}^{N}\left(\mathrm{x}_H^i + \alpha_j \cdot \frac{\mathcal{S}_j}{|\mathcal{S}_j|} + \sigma n_j\right) \quad (1)$$

where $\alpha_j(0, I_D)$ denotes the disturbance radius, $\mathcal{S}_j$ represents the normalized random direction vector, and σn_j indicates condition-related noise. This method dynamically adjusts the offset boundaries to account for changes in the feature distribution across different operating conditions. To adapt to the feature distribution of health state samples under diverse operating conditions, a condition-adaptive rejection probability p is employed to modify the offset boundaries enabling the generation of condition-specific out-of-distribution samples. The formula for the rejection probability is presented as follows:

$$p(d^*, d^-, \sigma) = \left(1 + \exp\left(\frac{d^* + d^-}{\sigma d^- k}\right)\right)^{-1} \quad (2)$$

where d^* represents the current offset distance and d^- denotes the historical minimum offset distance. As both d^* and d^- increase, the rejection probability p decreases along an S-shaped curve, ensuring a high probability when $d^* = 0$. Recommended parameters are $k = 7$ and $\sigma \in [0, 1]$, which control the softness of the boundary to ensure that the generated out-of-distribution samples form condition-adaptive pseudo-fault clusters along the outer edge of the health manifold. These samples, derived from an external distribution, are positioned in close proximity to the feature space occupied by health state samples, making them well suited for representing fault conditions. This nearness significantly boosts the accuracy of fault detection, particularly in cases where the model relies solely on health state data for training. By employing this technique, the samples produced within the external distribution samples $D_O(D_{\mathrm{O}}^1, D_{\mathrm{O}}^2, \cdots, D_{\mathrm{O}}^n)$ are placed beyond the boundaries of the health state feature space.

Finally, PFSL D_F is constructed by integrating the generic external samples D_E with the device-specific synthetic samples D_O. This hybrid composition is critical for generalization: while D_E introduces fault diversity, D_O compensates for device-to-device differences by anchoring the pseudo-faults to the target device's specific health distribution. This approach significantly boosts the model's fault detection capability and robustness, particularly in scenarios where training relies solely on health state samples.

Feature extractor

The residual shrinkage network (RSN) is pivotal in feature extraction, notably by reducing noise and improving the representativeness of the features. In contrast to traditional residual networks, RSN

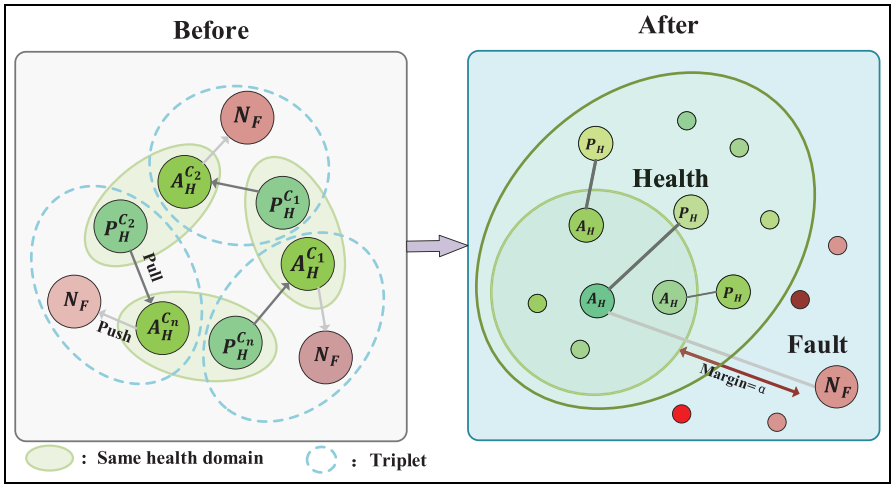

Figure 3. Schematic diagram of optimization with the UHDM.
UHDM: Unified health domain mechanism.

incorporates a soft thresholding function as a key element for filtering out irrelevant features.[27] This function is defined as follows:

$$Y = \begin{cases} x - \tau & \text{if } x > \tau \\ 0 & \text{if } -\tau \leqslant x \geqslant \tau \\ x + \tau & \text{if } x < -\tau \end{cases} \tag{3}$$

where x represents the input features, and Y denotes the output features. The soft thresholding mechanism selectively suppresses negative values, preserving only the most significant features, which are then passed forward for further processing. This approach also alleviates the issues of vanishing and exploding gradients—issues frequently encountered in deep networks—by ensuring gradient stability during backpropagation. The derivative of this soft thresholding function is expressed as follows:

$$\frac{\partial Y}{\partial x} = \begin{cases} 1 & \text{if } x > \tau \\ 0 & \text{if } -\tau \leqslant x \geqslant \tau \\ 1 & \text{if } x < -\tau \end{cases} \tag{4}$$

The RSN structure is designed with four units dedicated to residual shrinkage, each followed by a layer performing average pooling. Within every residual shrinkage unit, there exists a distinct component tasked with calculating the soft threshold. This component leverages global average pooling to assess the absolute values of the features, subsequently converting them into one-dimensional vectors. These vectors are then fed into a fully connected layer to derive scaling factors. To ensure these factors fall within the range [0,1], a sigmoid function is applied, defined as follows:

$$\alpha = \frac{1}{1 + e^{-z}} \tag{5}$$

where z represents the output from the fully connected layer. The threshold τ is calculated using the formula:

$$\tau = a \cdot average \left| x_{i,j,c} \right| \tag{6}$$

Here, $x_{i,j,c}$ indicates the feature at spatial position (i,j) and channel c. This threshold is fine-tuned to suppress noise effectively while safeguarding critical features. This configuration empowers the RSN to adeptly manage noisy data, ensuring dependable feature extraction. Consequently, the RSN can successfully derive feature sets $(g_H^1, g_H^2, \cdots, g_H^n)$ and $(g_F^1, g_F^2, \cdots, g_F^n)$ for the $D_H(D_H^1, \cdots, D_H^n)$ and D_F, respectively.

Unified health domain mechanisms

The UHDM is designed to minimize the distributional discrepancies of health states caused by varying operating conditions. The central concept involves introducing topological constraints based on the triplet loss function.[28] As depicted in Figure 3, raw health features under different operating conditions naturally reside in disparate domains, exhibiting significant distribution shift. To explicitly model cross-condition relationships and eliminate this bias, a specific triplet mining strategy is proposed, denoted as $\{A_H^{c_i}, P_H^{c_j}, N_F\}$. In this configuration, the anchor $A_H^{c_i}$ is a health sample randomly selected from a specific operating condition c_i, whereas the positive sample $P_H^{c_j}$ is deliberately drawn from a different operating condition c_j (where $i \neq j$). The

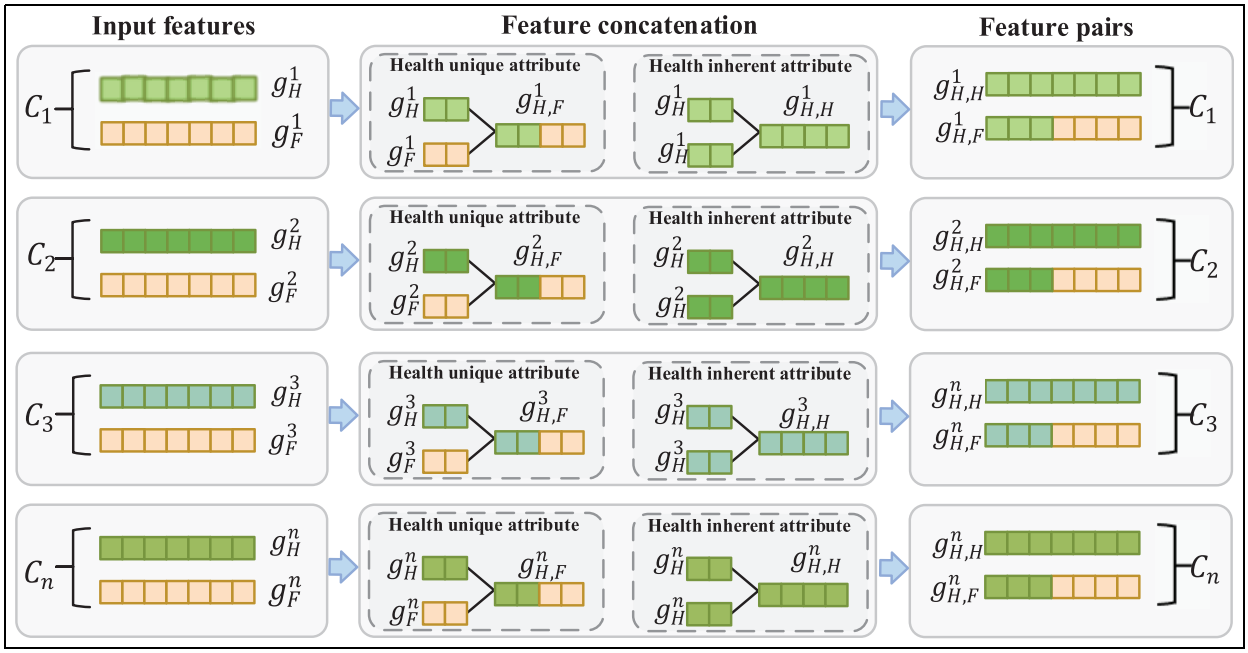

Figure 4. Feature concatenation mechanism.

negative sample N_F corresponds to a generated fault feature from the PFSL.

This cross-condition selection strategy is pivotal for reducing distribution shift. By enforcing the minimization of the distance between the anchor and the positive sample from disparate domains, the network is effectively penalized for retaining condition-specific information, such as features sensitive to speed or load variations. Instead, the model is compelled to extract condition-invariant health features that are shared across different operating conditions. Simultaneously, the negative sample ensures a clear separation from the fault boundary. Consequently, the anchor and positive samples—despite originating from different distributions—are drawn closer together. This process progressively merges the scattered health distributions into a compact, unified hypersphere, thereby effectively mitigating the distributional disparities and enhancing the model's robustness to unseen conditions. The triplet loss function is formally computed as follows:

$$\mathcal{L}_1 = L(A,P,N) = \max(0, d\left(A_H^{c_i}, P_H^{c_j}\right) - d(A_H^{c_i}, N_F) + \alpha) \tag{7}$$

where $d(\cdot,\cdot)$ denotes the calculation of the distance between two features. The loss function stipulates that the distance between the anchor and the positive sample must be smaller than the distance between the anchor and the negative sample, and that this difference must exceed the margin parameter α. The margin parameter plays a crucial role in defining the minimum separation between positive and negative samples. This prevents the model from converging to a trivial local optimum (where the positive sample is only marginally closer than the negative one) and encourages the learning of highly discriminative features, ensuring a robust separation between the unified health domain and the fault domain.

Health relation learning mechanism

The HRLM is designed to thoroughly explore the underlying relationships between health states across various operating conditions, thereby improving the model's robustness and adaptability in complex environments. Through the integration of feature pair concatenation and relation learning, HRLM effectively captures both the uniqueness and intrinsic nature of in health states, particularly under multiple operating conditions.

In the pair concatenation phase, HRLM introduces two innovative concatenation mechanisms that extract both unique and inherent features of health states. As shown in Figure 4, the first mechanism, health-fault feature concatenation, focuses on revealing the unique attribute of health states. By concatenating health features with PFSL features, the UHDRL is able to highlight the subtle differences between health state and

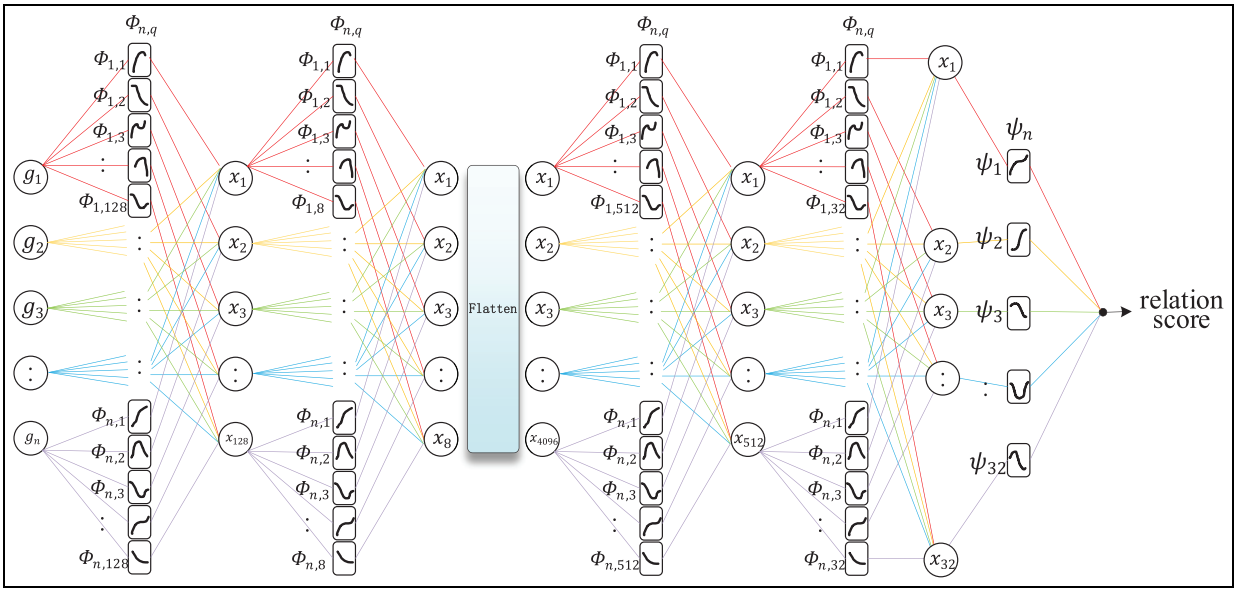

Figure 5. Kolmogorov–Arnold Network relation evaluator structure.

PFSL, providing a strong foundation for further analysis. The concatenated feature pairs are represented as follows:

$$g_{H,F} = \begin{cases} g^1_{H,F} = \oplus\left[g^1_H, g^1_F\right] \\ \vdots \\ g^n_{H,F} = \oplus\left[g^n_H, g^n_F\right] \end{cases} \tag{8}$$

where g^n_H represents the health features for the n-th condition, and g^n_F denotes the corresponding pseudo-fault features. This concatenation enables the model to effectively distinguish between health and fault states.

The second concatenation mechanism, health-health feature concatenation, aims to capture the inherent consistency within the health state, independent of specific fault scenarios. By concatenating each health feature with itself, this operation ensures that the UHDRL identifies the fundamental patterns of health states across conditions, unaffected by fault patterns. The concatenated mechanism is defined as follows:

$$g_{H,H} = \begin{cases} g^1_{H,H} = \oplus\left[g^1_H, g^1_H\right] \\ \vdots \\ g^n_{H,H} = \oplus\left[g^n_H, g^n_H\right] \end{cases} \tag{9}$$

This operation preserves the consistency of health states and helps the UHDRL maintain a stable understanding of health patterns.

In the relation learning phase, the HRLM uses the KANRE to uncover the intricate relationships between feature pairs. The KANRE progressively extracts these relationships through several layers of nonlinear transformations, as illustrated in Figure 5. Each layer propagates information by applying activation functions, which can be mathematically described as follows:

$$g_{(l+1,j)} = \sum_{i=1}^{n_l} \varphi_{(l,j,i)}\left(g_{(l,i)}\right) \tag{10}$$

where $g_{(l,i)}$ represents an iterative process where the output of each unit in a specific layer for the i-th unit in layer l, is processed using a tailored activation function $\varphi_{(l,j,i)}$. Through this iterative process, KANRE uncovers the complex relations between feature pairs, revealing both commonalities within health states and distinguishing features between health and pseudo-fault states. In KANRE, the activation function is a composite, blending a base function with a spline-based function, expressed mathematically as follows:

$$\phi(g) = \omega_b(g) + \omega_s \cdot \mathrm{spline}(g) \tag{11}$$

where ω_b and ω_s are the weights for the basis and spline functions, respectively. The basis function $b(g)$ is represented using the SiLU activation function:

$$\mathrm{SiLU}(g) = \frac{g}{1+e^{-g}} \tag{12}$$

The spline function spline (g), on the other hand, is formulated as a linear combination of B-spline basis functions:

$$\mathrm{spline}(g) = \sum_i c_i B_i(g) \tag{13}$$

where c_i are trainable coefficients, and $B_i(g)$ represents the i-th B-spline basis function. This dual-function approach allows KANRE to flexibly adjust its nonlinear responses according to the input features, boosting its adaptability and precision.

In the final relation score calculation, KANRE aggregates the information from previous layers through weighted summation, producing the final output. The relation score is computed as follows:

$$r = GELU\left(BN\left(Concat\left(\sum_{i=1}^{N} F_i \otimes g\right)\right)\right) \tag{14}$$

where $GELU$ is the activation function, BN represents batch normalization, $Concat$ denotes the concatenation operation, and $\otimes$ indicates the interaction between features. The resulting score r, which falls between 0 and 1, reflects the probability that the feature pair belongs to the same category. For each operating condition, a relation score matrix is generated, and these matrixes are subsequently merged into a comprehensive relation score matrix:

$$R_P = \begin{cases} r_P^1 = \begin{bmatrix} r_{H,F}^1 & \cdots & r_{H,F}^1 \\ r_{H,H}^1 & \cdots & r_{H,H}^1 \\ \vdots & \cdots & \vdots \\ r_{F,F}^1 & \cdots & r_{F,F}^1 \end{bmatrix} \\ \vdots \\ r_P^n = \begin{bmatrix} r_{H,F}^n & \cdots & r_{H,F}^n \\ r_{H,H}^n & \cdots & r_{H,H}^n \\ \vdots & \cdots & \vdots \\ r_{F,F}^n & \cdots & r_{F,F}^n \end{bmatrix} \end{cases} \tag{15}$$

where r_P^i refers to predicted relation score corresponding to operating condition C_i. The loss in the HRLM is determined by measuring the error between the actual relation score R_T and the predicted relation score R_P. The matrix structure that represents the actual relation score R_T is presented below:

$$R_T = \begin{cases} r_T^1 = \begin{bmatrix} 0 & \cdots & 0 \\ 1 & \cdots & 1 \\ \vdots & \cdots & \vdots \\ 1 & \cdots & 1 \end{bmatrix} \\ \vdots \\ r_T^n = \begin{bmatrix} 0 & \cdots & 0 \\ 1 & \cdots & 1 \\ \vdots & \cdots & \vdots \\ 1 & \cdots & 1 \end{bmatrix} \end{cases} \tag{16}$$

Subsequently, the error is then quantified via the mean squared error:

$$L_2 = \sum (R_P - R_T)^2 = \sum_{i=1}^{K} Loss_i = (r_P^i - r_T^i)^2 \tag{17}$$

Here, r_P^i denotes the predicted relation score and r_T^i the corresponding true score for the $i-th$ feature pair. The overall objective is obtained by summing these squared discrepancies over all K pairs.

Through this feature pair concatenation and relation learning strategy, HRLM effectively captures the deep relationships between health state and PFSL. This, in turn, enhances HRLM's capacity to identify and differentiate between various fault scenarios. This mechanism significantly enhances the HRLM's adaptability and robustness in dealing with complex data and varying operational conditions.

The fault detection framework base on UHDRL

A typical train transmission system comprises a traction motor, a driving gearbox, and two axle boxes. The limited availability of fault-related data, combined with the intricate mechanical couplings between these components, often hinders standalone systems from delivering precise fault detection and localization. To address this, a targeted fault detection strategy for each key component (traction motor, driving gearbox, and axle boxes) is proposed. Figure 6 illustrates the fault detection strategy based on UHDRL $\boldsymbol{S}(\mathcal{D}_H, \mathcal{D}_M; \theta)$. Sensors are strategically deployed on each crucial component to consistently track operational states. Real-time monitoring signals are collected from the K component and represented as $\mathcal{D}_M(\mathcal{D}_M^1, \mathcal{D}_M^2, \cdots, \mathcal{D}_M^K)$, where $\mathcal{D}_M^K$ corresponds to the K-th component's measurements. These monitoring signals are inherently uncertain and must undergo detection to identify potential faults. At the same time, historical health state samples, denoted as $\mathcal{D}_H(\mathcal{D}_H^1, \mathcal{D}_H^2, \cdots, \mathcal{D}_H^K)$, is utilized. Crucially, for each component K, the reference set $\mathcal{D}_H^K$ is constructed by random sampling from historical health data covering a wide spectrum of operating conditions.

Next, the feature extractor processes both the reference health samples $\mathcal{D}_H^K$ and the incoming monitoring signals $\mathcal{D}_M^K$. The resulting feature sets, denoted as g_H^K and g_M^K, represent the health and monitoring traits of the K-th component, respectively. These are combined into feature pairs $g_{H,M}^K$, which are evaluated by the KANRE to compute the relation scores $r_{\mathcal{D}_H^K, \mathcal{D}_M^K}^K$. This score quantifies the similarity between the monitoring features and the unified health domain. The scoring function for the UHDRL-based strategy is expressed as follows:

$$\boldsymbol{S}(\mathcal{D}_H, \mathcal{D}_M; \theta) = \boldsymbol{S}(\mathcal{D}_H^K, \mathcal{D}_M^K) \rightarrow r_{\mathcal{D}_H^K, \mathcal{D}_M^K}^K \tag{18}$$

Finally, the health status of each key component in the TTS is determined by comparing the relation score

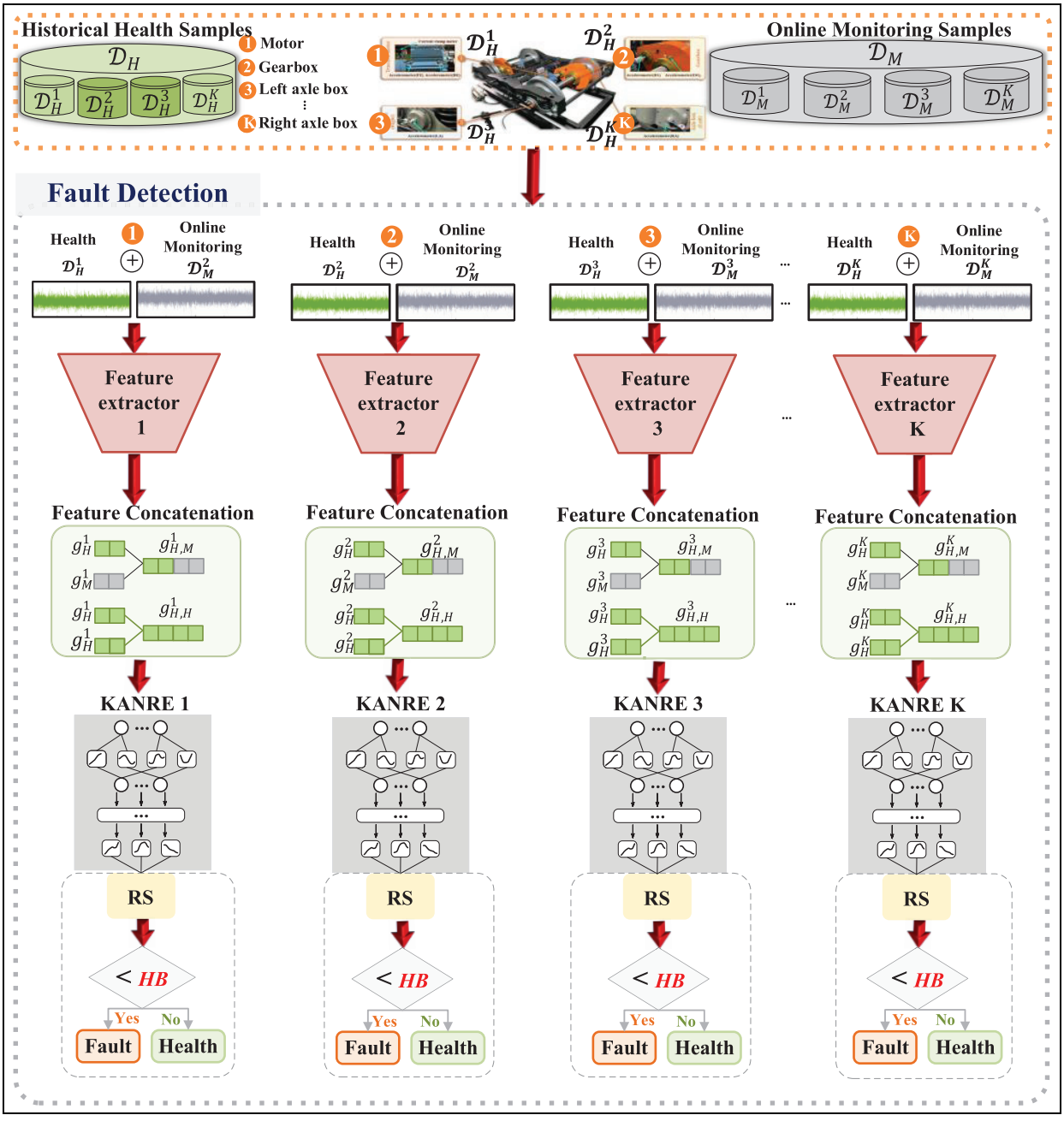

Figure 6. Train transmission systems fault detection framework base on UHDRL.
UHDRL: Unified health domain relation learning.

against a unified threshold. Since the domain shift caused by operating conditions has been mitigated, a single health baseline (HB) is sufficient for decision-making:

$$\begin{cases} Health, r^1_{\mathcal{D}_H^1, \mathcal{D}_M^1} \geqslant HB \\ \vdots \\ Fault, r^K_{\mathcal{D}_H^K, \mathcal{D}_M^K} < HB \end{cases} \tag{19}$$

where HB signifies the health baseline. Any $r^K_{\mathcal{D}_H^K, \mathcal{D}_M^K}$ meeting or exceeding HB indicates that the component resides within the unified health domain (Normal), whereas a score below HB flags a deviation, identifying a potential fault in the K-th key component.

Case study

To comprehensively evaluate the generalization performance and robustness of the proposed UHDRL

framework, experiments are conducted on three distinct datasets. These experiments are categorized based on the nature of their operating conditions: deterministic and stochastic.

Deterministic operating conditions (cases 1 and 2) refer to scenarios where operating parameters are discrete, predefined, and consistent across both health and fault states. The distribution of operating conditions for fault samples aligns strictly with that of the health samples. Stochastic operating conditions (Case 3) refer to more complex scenarios characterized by random variations and structural discrepancies. In this setting, not only do the operating parameters differ between health and fault states but different axle system models are also employed for different fault modes. This introduces a compound domain shift caused by both parameter mismatch and hardware variation.

Case 1: Metro train bogie transmission system under deterministic operating conditions

Dataset description. To validate the proposed UHDRL's effectiveness, a metro train bogie transmission system (MTBTS) operating under deterministically varying operating conditions is utilized.[1] As depicted in Figure 7(a), the fault simulation test bench for the MTBTS is a scaled-down and simplified version of a real metro bogie at a 1:2 ratio. The test bench features a single-power transmission chain consisting of a motor, a reduction gearbox, and an axle box. This transmission chain is driven by a three-phase asynchronous AC motor, with its speed controllable via a frequency converter. The load is applied using a hydraulic device. In this system, the motor bearing model is SKF 6205-2RSH; the reduction gearbox employs helical gears, featuring 16 teeth on the driving component and 107 on the driven one; the support bearing supporting the driving gear is designated as HRB 32305, and the bearing within the axle box is identified as HRB 352213.

Table 1 illustrates that the dataset for the MTBTS encompasses samples under nine different operating conditions for each state type, simulating a range of train operating scenarios. All nine operating conditions involve deterministic variations, aligning with the operating conditions corresponding to the health state types. Variations in motor speeds represent different train speeds, while varying lateral loads simulate both straight and curved train movements. A positive lateral load indicates that the loading direction points toward the motor side of the transmission chain, whereas a negative load points toward the gearbox side. To investigate different fault conditions, three experimental modes are conducted: single fault mode, component-level compound fault mode, and system-level compound fault mode. As outlined in Table 2, a total of 50 fault modes are simulated, including 16 single faults, 10 compound faults at the component level, and 24 compound faults at the system level. Each fault mode is tested under 9 operating conditions, resulting in 459 fault experiments. Vibration sensors recorded data at a sampling rate of 64 kHz, with each run lasting 120 s. In every experiment, 1000 fault samples and 2000 health samples are captured, with each sample consisting of 2048 time-domain points. For model development, 800 health samples are utilized for training and 200 for validation. The test set contains 1000 samples encompassing both health and fault states.

The PFSL comprises external equipment fault samples and out-of-distribution samples. The external equipment fault samples, serving as pseudo-fault samples, are sourced from the gearbox test bench and Paderborn University,[29] totaling 48 fault states. The gearbox test rig, shown in Figure 8, can simulate 14 different fault scenarios, including 6 single faults and 8 compound faults. The single faults include broken teeth, missing teeth, cracked teeth, coupling looseness, bearing roller wear, and bearing outer ring wear. Additionally, the test rig can replicate compound faults, such as combinations of broken teeth with missing teeth, cracked teeth, coupling looseness, bearing roller wear, or bearing outer ring wear. It also supports scenarios where missing teeth occur alongside coupling looseness, bearing roller wear, or bearing outer ring wear. The fault types in the Paderborn University dataset include man-made faults and naturally occurring faults. It includes faults in the inner and outer rings, with both artificial and real defects, resulting in a total of 32 distinct fault types. Additionally, 15 out-of-distribution samples are generated. All PFSL are used exclusively as training samples.

Detection results under single-fault mode. The UHDRL is trained with a learning rate set at 0.001, data processed in batches size of 8, and Adam optimization. Prior to employing UHDRL for identifying faults within the transmission system of a metro train bogie, it is essential to establish the HB value. The HB values are considered within the interval of 0.9 to 0.99, and the most suitable value for each critical component is determined through analysis of the validation data. Figure 9 presents the mean accuracy of fault detection across various HB settings using the validation data, where each HB value undergoes ten evaluation trials. The findings demonstrate that UHDRL maintains an accuracy exceeding 90% across the entire range of HB values. Notably, at an HB value of 0.95, the accuracy in detecting faults is uniformly high across all critical

Figure 7. (a) Experimental platform of MTBTS (b) Motor fault types (c) Gearbox fault types (d) Axlebox fault types.
MTBTS: Metro train bogie transmission system.

Table 1. Deterministic operating condition setting.

Operating condition	Motor speed/transverse load	Operating condition	Motor speed/transverse load
WC1	20 Hz/0 kN	WC6	60 Hz/+10 kN
WC2	40 Hz/0 kN	WC7	20 Hz/−10 kN
WC3	60 Hz/0 kN	WC8	40 Hz/−10 kN
WC4	20 Hz/+10 kN	WC9	60 Hz/−10 kN
WC5	40 Hz/+10 kN		

components, thus establishing 0.95 as the most effective *HB* value.

First, the capability of UHDRL in detecting single-fault modes under varying operating conditions is

Table 2. State type for MTBTS.

Mode	Fault location	Fault type	Fault code
Single fault	Motor	Health	M0
		Short circuit	M1
		Broken rotor bar	M2
		Bearing fault	M3
		Bowed axis	M4
	Gearboxes	Health	G0
		Gear cracked tooth	G1
		Gear worn tooth	G2
		Gear missing tooth	G3
		Gear chipped tooth	G4
		Bearing inner race fault	G5
		Bearing outer race fault	G6
		Bearing rolling element fault	G7
		Bearing cage fault	G8
	Left axle boxes	Health	LA0
		Bearing inner race fault	LA1
		Bearing outer race fault	LA2
		Bearing rolling element fault	LA3
		Bearing cage fault	LA4
	Right axle boxes	Health	RA0
Component-level compound-fault	Gearboxes	Gear cracked tooth, bearing inner race fault	G1 + G5
	Gearboxes	Gear worn tooth, bearing inner race fault	G2 + G5
	Gearboxes	Gear missing tooth, bearing inner race fault	G3 + G5
	Gearboxes	Gear chipped tooth, bearing inner race fault	G4 + G5
	Left axle box	Bearing inner race fault, bearing outer race fault	LA1 + LA2
	Left axle box	Bearing outer race fault, bearing rolling element fault	LA2 + LA3
	Left axle box	Bearing outer race fault, bearing cage fault	LA2 + LA4
	Left axle box	Bearing inner race fault, bearing outer race fault, bearing rolling element fault	LA1 + LA2 + LA3
	Left axle box	Bearing inner race fault, bearing outer race fault, bearing cage fault	LA1 + LA2 + LA4
	Left axle box	Bearing inner race fault, bearing outer race fault, bearing rolling element fault, bearing cage fault	LA1 + LA2 + LA3 + LA4
System-level compound-fault	Motor, gearbox	Short circuit, gear missing tooth	M1 + G3
	Motor, gearbox	Short circuit, bearing inner race fault	M1 + G5
	Motor, gearbox	Broken rotor bar, gear missing tooth	M2 + G3
	Motor, gearbox	Broken rotor bar, bearing inner race fault	M2 + G5
	Motor, gearbox	Bearing fault, gear missing tooth	M3 + G3
	Motor, gearbox	Bearing fault, bearing inner race fault	M3 + G5
	Motor, gearbox	Bowed axis, gear missing tooth	M4 + G3
	Motor, gearbox	Bowed axis, bearing inner race fault	M4 + G3
	Motor, left axle box	Short circuit, bearing inner race fault	M1 + LA1
	Motor, left axle box	Broken rotor bar, bearing inner race fault	M2 + LA1
	Motor, left axle box	Bearing fault, bearing inner race fault	M3 + LA1
	Motor, left axle box	Bowed axis, bearing inner race fault	M4 + LA1
	Gearbox, left axle box	Gear missing tooth, bearing inner race fault	G3 + LA1
	Left axle box, right axle box	Bearing inner race fault, bearing inner race fault	LA1, RA1

(continued)

Table 2. Continued

Mode	Fault location	Fault type	Fault code
	Motor, gearbox, left axle box	Short circuit, gear missing tooth, bearing inner race fault	M1 + G3 + LA1
	Motor, gearbox, left axle box	Short circuit, bearing inner race fault, bearing inner race fault	M1 + G5 + LA1
	Motor, gearbox, left axle box	Broken rotor bar, gear missing tooth, bearing inner race fault	M2 + G3 + LA1
	Motor, gearbox, left axle box	Broken rotor bar, bearing inner race fault, bearing inner race fault	M2 + G5 + LA1
	Motor, gearbox, left axle box	Bowed axis, gear missing tooth, bearing inner race fault	M4 + G3 + LA1
	Motor, gearbox, left axle box	Bowed axis, bearing inner race fault, bearing inner race fault	M4 + G5 + LA1
	Motor, left axle box, right axle box	Short circuit, bearing inner race fault, bearing inner race fault	M1 + LA1 + RA1
	Motor, left axle box, right axle box	Broken rotor bar, bearing inner race fault, bearing inner race fault	M2 + LA1 + RA1
	Motor, gearbox, left axle box, right axle box	Short circuit, gear missing tooth, bearing inner race fault, bearing inner race fault	M1 + G5 + LA1 + RA1

MTBTS: Metro train bogie transmission system.

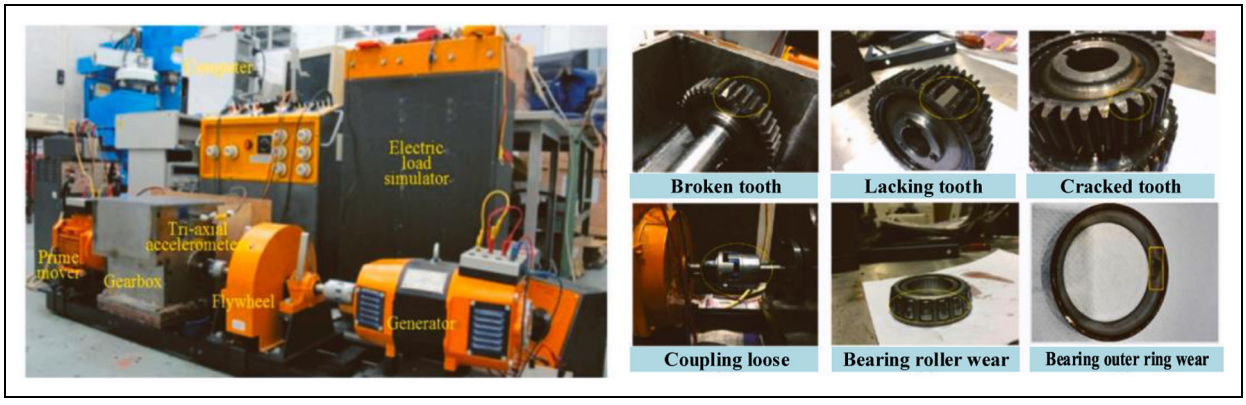

Figure 8. Gearbox test bench for external equipment faults as part of the generation of pseudo-fault data.

evaluated. The results, averaged over ten trials to ensure statistical reliability, are summarized in Figure 10. The UHDRL achieves an impressive detection accuracy ranging from 86.91% to 97.41% across most of the nine operating conditions. This superior performance validates the efficacy of the UHDM, which successfully extracts condition-invariant health features, enabling precise boundary alignment even in the absence of target fault samples. For instance, the left axle box bearing maintains over 90% accuracy across all operating conditions. Further granular analysis reveals that nearly all specific fault types within this component surpass the 90% threshold. However, performance fluctuations are observed in specific scenarios. The fault type LA1 under condition WC1 records a lower accuracy of 66.4%, and notably, the motor fault type M1 under WC1 drops to 27.15%. This significant dip suggests that under specific operating conditions (like WC1), the feature signatures of certain faults (M1) exhibit a high degree of overlap with the generalized health domain, posing a challenge for anomaly differentiation. Despite these localized limitations, the average detection accuracy for motor faults remains above 75%, with the majority exceeding 90%. These findings confirm that while extreme spectral overlap can affect specific cases, UHDRL effectively mitigates the global impact of distribution shifts, delivering robust overall performance.

Figure 11 shows the feature distribution of various state types via t-SNE. It is evident that health state

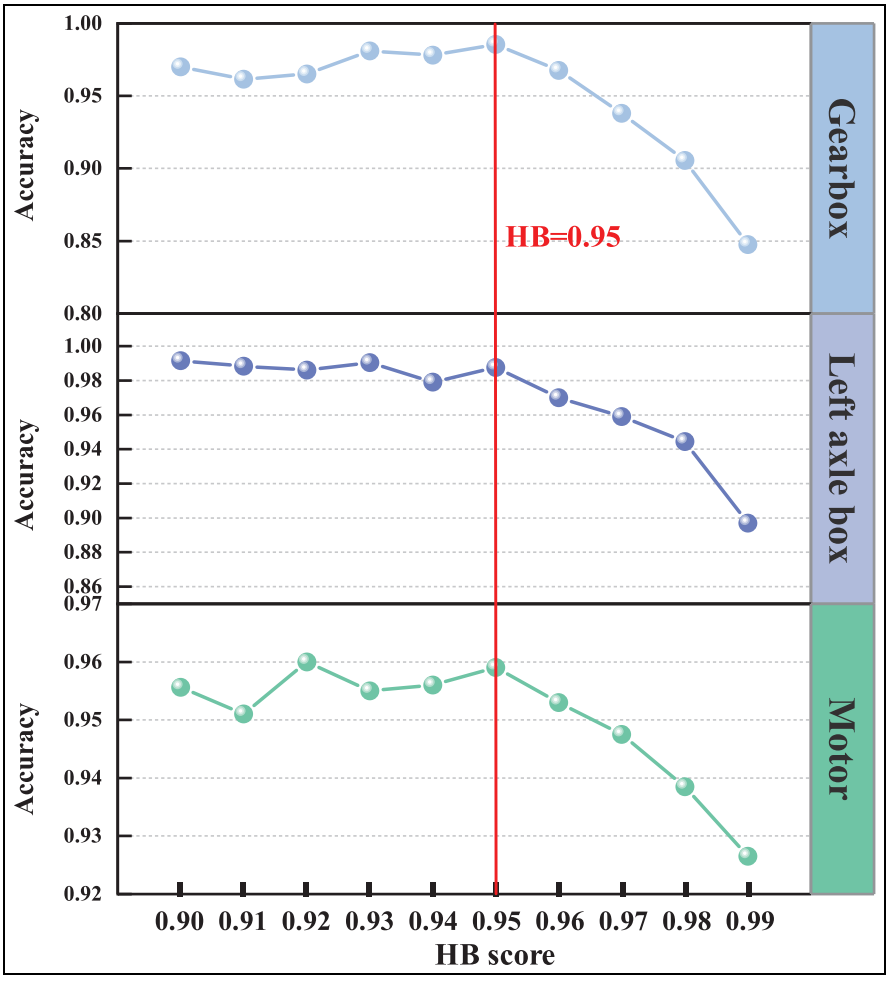

Figure 9. Determination of the UHDRL HB value for MTBTS.
HB: Health baseline; UHDRL: Unified health domain relation learning; MTBTS: Metro train bogie transmission system.

features extracted from nine distinct operating conditions are not scattered but are successfully compressed into a single, compact region. In sharp contrast, features from various fault types are distinctly separated from this unified health manifold. This visualization provides compelling evidence that the UHDM strategy effectively aligns diverse health distributions into a consistent health representation. By minimizing the intra-class variance of health states caused by operating condition changes, UHDRL significantly reduces the domain shift, thereby ensuring a reliable decision boundary for fault detection.

Figure 12 further illustrates the relation scores of state types for each component under different operating conditions. The relation scores, spanning a range of 0–1, are depicted via a color gradient shifting from red to green. Red denotes a fault state, while green indicates operational normalcy. Typically, the color distribution exhibits a sharp contrast, leaning heavily toward either deep red or distinct green. This clear separation highlights the effectiveness of the HRLM in precisely distinguishing between fault and health states. Typically, accurate detections are represented by a dominant color consistency (e.g., fault samples appearing strictly red). However, certain scenarios reveal a blend of red and green hues (intermediate scores), most notably for the motor fault type M1 under operating condition WC1. In this specific case, the predominance of green hues—where red was expected—correlates with a detection accuracy of only 27.31%. This indicates that the model misclassified these specific fault features as health states (high relation scores), exposing a limitation of UHDRL's performance under specific, highly overlapping conditions. Despite such isolated challenges, the approach excels in the vast majority of cases. By leveraging its capacity to detect nuanced differences based on the relation score intensity, UHDRL ensures robust fault identification. Overall, the results

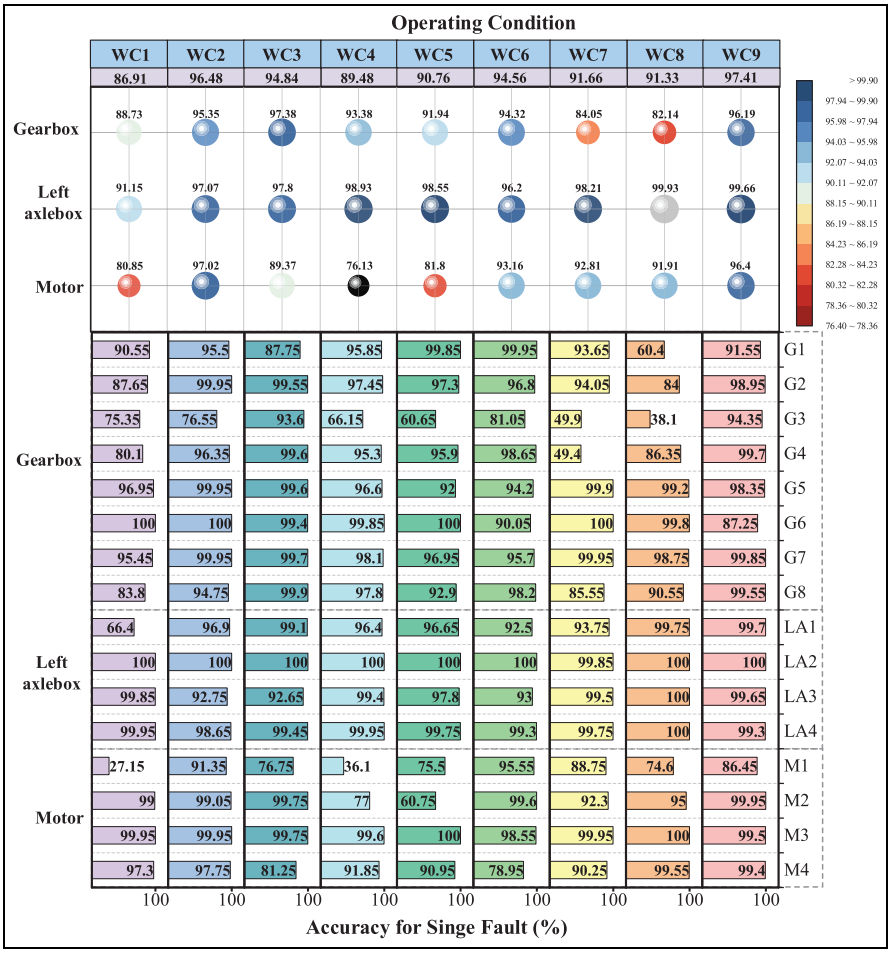

Figure 10. Detection results for single fault modes under various operating conditions of MTBTS.
MTBTS: Metro train bogie transmission system.

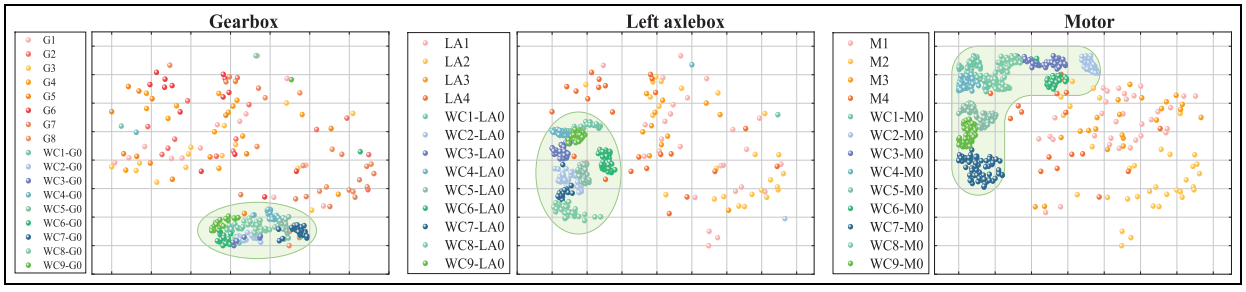

Figure 11. Feature distribution of state type under different operating conditions.

demonstrate that UHDRL successfully mitigates the impact of data distribution shifts caused by varying operating conditions.

Detection results under compound-fault mode. To further validate the effectiveness of the UHDRL under different operating conditions, a variety of compound-fault scenarios are tested. In real-world contexts, compound-fault situations frequently arise, featuring multiple fault types within one component, termed component-level compound-faults, or simultaneous faults spanning several components, identified as system-level compound-faults. According to Table 2,

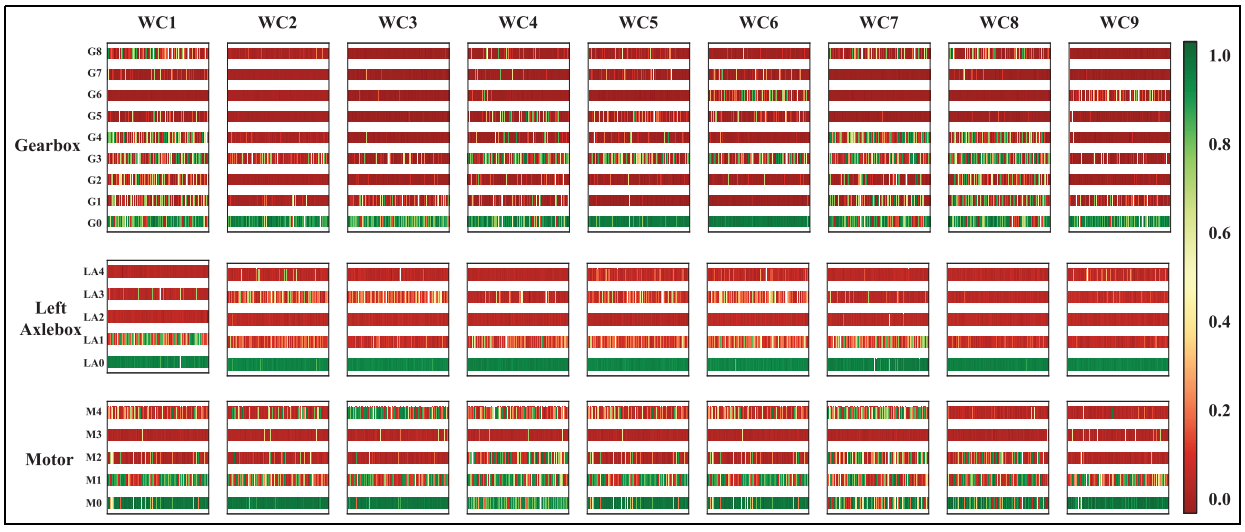

Figure 12. Relation scores for different states type under different operating conditions.

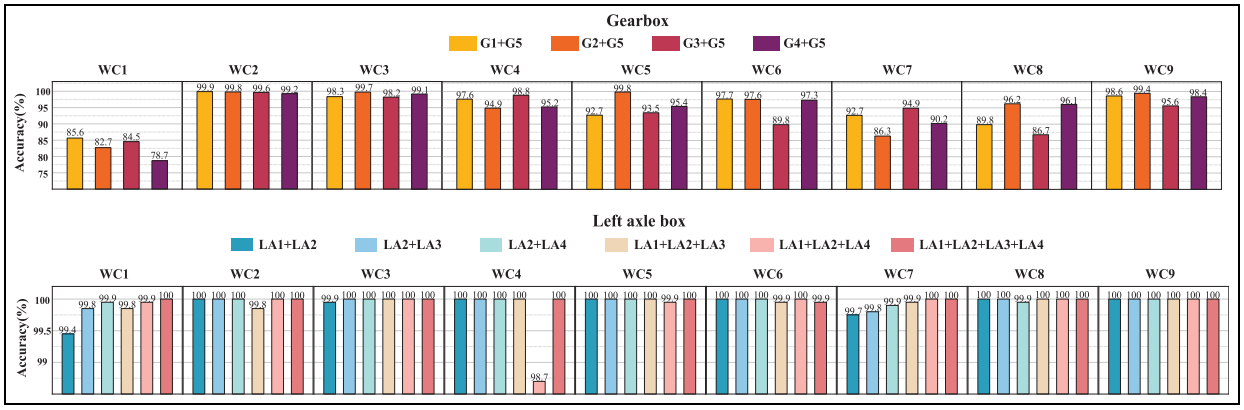

Figure 13. Detection results for component-level compound-fault modes under various operating conditions.

these compound-faults are organized into categories based on their occurrence at the component or system level.

Figure 13 illustrates the detection accuracy of the UHDRL for component-level compound-faults under different operating conditions. The results indicate that the UHDRL successfully detects faults in two-class, three-class, and four-class compound-fault scenarios with high accuracy. Specifically, for left axle box under different operating conditions, the detection accuracy for compound-fault types exceeds 98% in most cases, demonstrating that UHDRL can effectively handle the combined impact of multiple fault types. However, some lower detection accuracy is observed, such as in the gearbox G4 + G5 compound-fault type under operating condition WC1, where the detection accuracy is only 78.7%. This suggests that while UHDRL performs excellently in most conditions, there is still some error in specific situations. Nonetheless, overall, UHDRL achieves a detection accuracy above 90% for gearbox compound-faults under various operating conditions.

Further analysis of the system-level compound-fault detection results in Table 3 supports the effectiveness of the UHDRL. Whether for simple component-level compound-faults or more complex system-level compound-faults, the detection accuracy of UHDRL consistently exceeds 90%, with an average accuracy of 97.76% in some cases. This demonstrates that the UHDRL is capable of effectively handling complex fault modes under varying operating conditions, ensuring high-precision fault detection. Moreover, the detection accuracy for compound-faults is generally higher than for single faults, which is understandable. The

Table 3. Detection accuracy for system-level compound-fault modes under various operating conditions.

Operating conditions		WC1	WC2	WC3	WC4	WC5	WC6	WC7	WC8	WC9	Avg
Fault type	M1 + G3	93.63	99.95	99.50	98.58	99.28	99.20	96.75	93.38	97.57	97.54
	M1 + G5	91.50	99.55	99.18	99.15	98.63	97.83	97.53	94.35	96.45	97.13
	M2 + G3	92.18	99.63	99.93	98.15	98.95	99.78	94.95	97.03	99.52	97.79
	M2 + G5	95.18	99.85	99.75	98.50	98.98	99.63	93.45	98.53	99.28	98.13
	M3 + G3	88.85	100.00	98.53	99.05	99.63	99.20	99.48	94.68	96.78	97.35
	M3 + G5	92.60	99.95	99.78	98.60	98.90	99.38	94.98	96.68	99.38	97.80
	M4 + G3	98.28	99.80	99.38	99.55	99.53	99.70	96.88	96.48	98.43	98.67
	M4 + G5	90.70	96.93	98.28	95.80	96.65	98.78	94.20	95.53	99.58	96.27
	M1 + LA1	91.63	96.33	99.13	96.30	97.73	98.95	97.20	99.93	99.98	97.46
	M2 + LA1	92.90	98.93	99.93	99.48	99.70	99.53	96.68	99.78	99.83	98.53
	M3 + LA1	98.63	97.98	99.93	97.60	99.95	99.80	98.33	99.85	99.98	99.11
	M4 + LA1	93.60	97.05	99.80	99.53	99.90	99.83	97.40	99.98	100.00	98.56
	G3 + LA1	90.38	99.68	99.10	96.93	98.60	99.35	95.65	94.43	97.43	96.84
	LA1 + RA1	100.00	100.00	100.00	100.00	100.00	100.00	99.90	100.00	100.00	99.99
	M1 + G3 + LA1	87.48	96.65	98.52	97.15	98.16	97.67	96.73	94.75	97.52	96.07
	M1 + G5 + LA1	93.55	97.77	98.63	96.17	98.40	98.25	95.32	94.83	97.38	96.70
	M2 + G3 + LA1	91.40	98.88	99.63	98.15	99.12	99.20	95.95	98.35	99.73	97.82
	M2 + G5 + LA1	90.02	98.98	99.10	96.48	98.80	98.42	94.78	98.00	99.23	97.09
	M4 + G3 + LA1	99.93	99.55	98.77	99.38	98.03	98.75	99.18	95.63	98.57	98.64
	M4 + G5 + LA1	93.22	97.92	99.43	97.57	99.30	98.57	98.07	97.43	99.10	97.84
	M1 + LA1 + RA1	92.85	98.23	99.80	94.25	98.88	99.70	97.60	99.45	100.00	97.86
	M2 + LA1 + RA1	99.80	99.75	99.83	99.98	100.00	100.00	99.78	99.90	100.00	99.89
	M1 + G5 + LA + RA1	99.70	98.05	99.88	98.98	97.27	96.98	99.92	99.05	99.45	98.81
	M4 + G3 + LA1 + RA1	97.60	99.93	99.55	99.50	99.18	99.73	99.05	97.98	99.48	99.11
Avg		93.98	98.80	99.39	98.12	98.90	99.09	97.07	97.33	98.94	97.96

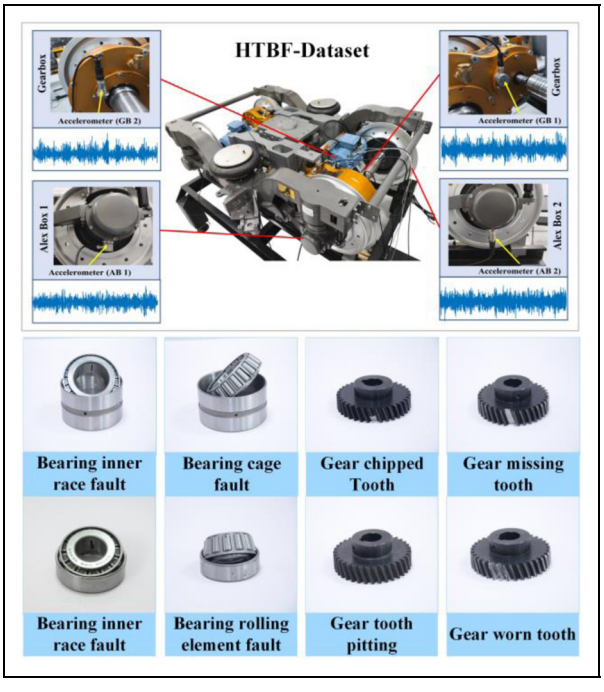

Figure 14. Experimental platform of HSTB.
HSTB: high-speed train bogie.

compound-faults typically generate stronger fault signals, which more clearly differentiate the health state from the faulty state compared to single fault modes, thus improving detection accuracy. Overall, the experimental results further confirm that the UHDRL method can effectively detect faults in compound-fault scenarios under different operating conditions, showcasing its robustness and superiority in varying operational environments.

Case 2: High-speed train bogie under deterministic operating conditions

Figure 14 shows the high-speed train bogie (HSTB) fault simulation rig. The rig's main components include the frame, motor, gearbox, main shaft, wheelset, and axlebox. The testbed allows replacement of faulty bearings and gears in the driveline to reproduce a variety of fault conditions. As summarized in Table 4, the resulting dataset comprises 29 state types spanning three categories: gearbox faults, axlebox faults, and compound faults. The axlebox and gearbox bearings each contain four fault modes, namely rolling element fault, inner-race fault, outer-race fault, and cage fault. Gear faults include tooth missing, broken tooth, pitting, and tooth surface wear. All faults were introduced artificially by wire-cutting and graded by damage severity. Representative photos of the simulated faults for each component are shown in Figure 14. The test campaign

Table 4. State type for HSHB.

Mode	Fault location	Fault type	Fault severity level	Fault dimensions	Fault code
Single fault	Axleboxes	Health	/	/	H
		Rolling element	Level 1	4 × 0.2 × 0.7	RE1
			Level 2	11 × 0.5 × 0.7	RE2
			Level 3	22 × 0.8 × 0.7	RE3
		Inner race	Level 1	15 × 0.2 × 0.7	IR
		Outer race	Level 1	4 × 0.2 × 0.7	OR1
			Level 2	11 × 0.5 × 0.7	OR2
			Level 3	22 × 0.8 × 0.7	OR3
		Cage creaking	Radial notch	/	CC
	Gearboxes	Rolling element	Level 1	3.5 × 0.1 × 0.5	RE1
			Level 2	8.5 × 0.3 × 0.5	RE2
			Level 3	17 × 0.5 × 0.5	RE3
		Inner race	Level 1	15 × 0.2 × 0.7	IR
		Outer race	Level 1	4.5 × 0.1 × 0.5	OR1
			Level 2	9 × 0.3 × 0.5	OR2
			Level 3	19 × 0.5 × 0.5	OR3
		Cage creaking	Radial notch	/	CC
Compound-fault	Fault type			Fault code	
	Breaking off gear tooth (BG) and gear surface wear (GW2)			BG + GW2	
	BG and gearboxes OR3			BG + OR3	
	NG and GW2			NG + GW2	
	Gear RC and GW2			RC + GW2	

HSTB: high-speed train bogie; NG: Notched gear; RC: Root ceack.

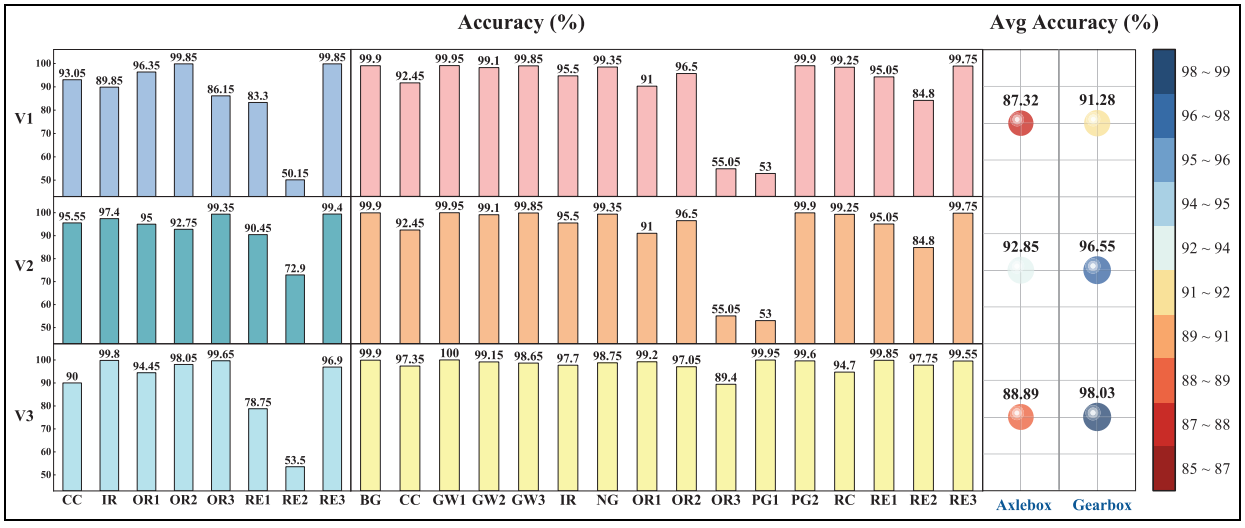

Figure 15. Detection results for single fault modes under various operating conditions of HSTB.
HSTB: high-speed train bogie.

covers three operating conditions to emulate different train speeds. Under a constant load of 1200 kg, the motor speed was adjusted to produce operating frequencies of 30 Hz, 40 Hz, and 50 Hz, denoted V1, V2 and V3, respectively. Vibration signals were sampled at 25.6 kHz. Data construction and preprocessing follow the same protocol as case 1.

Figure 15 presents the fault detection accuracy rates for various single fault types of the HSTB under diverse operating conditions. The experimental results demonstrate that UHDRL sustains an average accuracy exceeding 87% for both components across all tested conditions. Notably, the detection precision for the gearbox peaks at 98.03% under operating condition

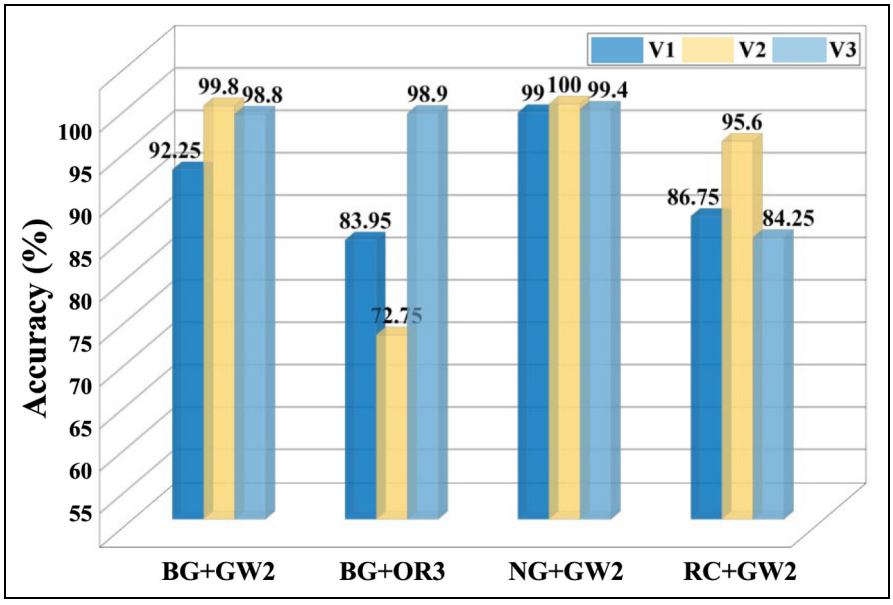

Figure 16. Detection results for c compound-fault modes under various operating conditions.

Figure 17. Experimental platform of high-speed train axle box bearing.

V3. This suggests that higher operating speeds may enhance the separability of fault features, allowing the model to capture more distinctive impulsive signatures. While the vast majority of single fault modes attain high diagnostic accuracy (nearly all above 90%), a few isolated cases exhibit suboptimal performance, likely due to feature masking effects in specific low-severity scenarios.

Furthermore, the robustness of UHDRL extends to the more challenging task of compound fault diagnosis. As depicted in Figure 16, the detection accuracy for most compound fault modes surpasses 90%. This indicates that the model is capable of effectively disentangling complex coupled fault features. Collectively, these results substantiate that UHDRL effectively mitigates the distribution shifts caused by varying operating conditions. By constructing a unified and compact representation of health states, the framework achieves consistent and robust fault detection performance even under complex interference.

Case 3: High-speed train axle box bearing under nondeterministic operating conditions

To further validate the effectiveness of the proposed UHDRL, a high-speed train axle box bearing (HSTAB) test rig is used for testing. As shown in Figure 17, the test rig primarily consists of a traction motor, universal coupling, spindle, test rig frame, test bearing, and support bearings. The rig is driven by a variable-frequency three-phase motor, which provides rotational power, and is connected to the entire axle

Table 5. State type for high-speed train axle box bearing.

Mode	Sate type	Bearing type	Shaker frequency	Static load (kg)	Speed (r / min)	Fault code
Single Fault	Health	1639185–24	0	100	100	H-1
	Health	1639185–24	0	100	500	H-2
	Health	1639185–24	0	100	800	H-3
	Health	1639185–24	0	100	1100	H-4
	Health	1639185–24	0	100	1400	H-5
	Inner ring abrasion	0147AB	5	100	100	IA-1
	Inner ring abrasion	0147AB	5	100	300	IA-2
	Inner ring abrasion	0147AB	5	100	500	IA-3
	Inner ring abrasion	0147AB	5	100	800	IA-4
	Inner ring abrasion	0147AB	5	100	1100	IA-5
	Inner ring wear	1472	5	100	100	IW-1
	Inner ring wear	1472	5	100	500	IW-2
	Inner ring wear	1472	5	100	800	IW-3
	Inner ring wear	1472	5	100	1100	IW-4
	Inner ring wear	1472	5	100	1400	IW-5
	Outer ring abrasion	1296AB	10	100	100	OA-1
	Outer ring abrasion	1296AB	10	100	500	OA-2
	Outer ring abrasion	1296AB	10	100	800	OA-3
	Outer ring abrasion	1296AB	10	100	1100	OA-4
	Outer ring abrasion	1296AB	10	100	1400	OA-5
	Outer ring wear	0985B	5	100	100	OW-1
	Outer ring wear	0985B	5	100	500	OW-2
	Outer ring wear	0985B	5	100	800	OW-3
	Outer ring wear	0985B	5	100	1100	OW-4
	Outer ring wear	1463A	0	0	100	OW-5
	Rolling body wear	1463A	0	0	300	RW-1
	Rolling body wear	1463A	0	0	500	RW-2
	Rolling body wear	1463A	0	0	800	RW-3
	Rolling body wear	1463A	5	0	100	RW-4
	Rolling body wear	1463A	5	100	1400	RW-5
	Cage fault	1296A/B	10	1000	1200	CF
Compound-fault	Inner ring and outer ring faults	1472A (B)	5	100	500	IOF-1
	Inner ring and outer ring faults	1472A (B)	5	100	800	IOF-2
	Inner ring and outer ring faults	1472A (B)	5	100	1100	IOF-3
	Inner ring and outer ring faults	1472A (B)	5	100	1400	IOF-4
	Inner ring and rolling body faults	1280AB	5	500	1400	IRF-1
	Inner ring and rolling body faults	1280AB	10	500	800	IRF-2
	Inner ring and rolling body faults	1280AB	5	500	1100	IRF-3
	Inner ring and rolling body faults	1280AB	5	500	800	IRF-4
	Inner ring and rolling body faults	1280AB	5	500	500	IRF-5

box bearing system through the universal coupling. Different static loads can be applied to the test bearing. As shown in Table 5, the test simulates different operating conditions by adjusting the bearing's rotational speed, static load, shaker frequency, and bearing type, while simulating various fault modes under these conditions. A total of six single fault modes and two compound-fault modes are tested. It is found that the operating conditions for different fault modes are significantly different from those under health states, and the characteristics of the operating conditions for each fault mode are different. This indicates that the operating conditions of the HSTAB are nondeterministic. The setup for the PFSL, training samples and testing samples is the same as in the scenario of case 1.

Experiments similarly reveal that the optimal *HB* value for the HSTAB is set to 0.95. Table 6 presents the fault detection accuracy for various fault types under these stochastic conditions. The results reveal that UHDRL achieves a robust detection accuracy of 90.03% for single fault modes and an average of 86.96% for compound-fault modes. For the majority of stochastic conditions, the accuracy exceeds 90%. This validates that UHDRL effectively reduces the

Table 6. Detection accuracy for high-speed train axle box bearing under nondeterministic operating conditions.

Fault type	Fault code	Accuracy	Avg	Fault type	Fault code	Accuracy	Avg
Single Fault: 90.03							
Inner ring abrasion	IA-1	58.1	81.13	Inner ring wear	IW-1	97.05	98.54
	IA-2	92.35			IW-2	99.3	
	IA-3	98.4			IW-3	99.45	
	IA-4	93.6			IW-4	99.9	
	IA-5	63.2			IW-5	97	
Outer ring abrasion	OA-1	93.3	89.24	Outer ring wear	OW-1	93.75	96.19
	OA-2	80.75			OW-2	87.3	
	OA-3	90.2			OW-3	100	
	OA-4	95.2			OW-4	99.95	
	OA-5	86.75			OW-5	99.95	
Rolling body wear	RW-1	96.8	82.45	Cage fault	CF	92.61	92.61
	RW-2	47.6					
	RW-3	82.1					
	RW-4	95.25					
	RW-5	90.5					
Compound-fault: 86.96							
Inner ring and outer ring faults	IOF-1	60.85	82.47	Inner ring and rolling body faults	IRF-1	59.15	90.56
	IOF-2	80.11			IRF-2	96.45	
	IOF-3	94.7			IRF-3	99.6	
	IOF-4	94.2			IRF-4	98.7	
					IRF-5	98.9	

impact of severe distribution shifts caused by unaligned operating parameters, successfully generalizing the unified health boundary to unseen domains. However, performance variability is observed. Notably, for the fault code IA-1, the detection accuracy drops to 58.1%. This substantial decline suggests that for this specific fault type and condition combination, the generated fault features exhibit a high degree of similarity to the unified health features, leading to feature confusion within the decision boundary. Additionally, the slightly lower accuracy for compound faults (86.96%) reflects the increased difficulty in decoupling overlapping fault signatures under stochastic interference. Overall, the results demonstrate that while extreme feature overlap poses challenges in isolated cases, UHDRL effectively mitigates the global domain shift posed by varying operating conditions, achieving robust fault detection through the unified representation of health states.

Result discussion

Ablation analysis. To quantify the contributions of UHDM and HRLM within the proposed UHDRL framework, ablation experiments were performed by removing each module in turn. Figure 18 reports detection performance on three datasets after removing UHDM or HRLM. The results indicate that omission of either module leads to a substantial drop in detection accuracy across all operating conditions. The impact is most pronounced when HRLM is removed, which suggests that the detection pipeline strongly depends on HRLM because it plays a critical role in assessing similarity between healthy and faulty states. Moreover, the performance degradation under nondeterministic operating conditions (HSTAB) is generally larger than that observed under deterministic conditions. This difference arises because the distribution gap between healthy and faulty samples is greater under nondeterministic conditions; without UHDM to map healthy samples from different conditions into a common space, distinguishing faults becomes considerably harder. These findings confirm the necessity and complementarity of UHDM and HRLM for ensuring UHDRL's robustness across varying operating conditions.

Impact of the number of PFSL types on UHDRL. This section examines how the size of the external PFSL affects UHDRL's anomaly detection performance. As illustrated in Figure 19, there is a clear positive correlation between detection accuracy and the diversity of PFSL types. The results reveal a crucial insight regarding device-to-device differences: although external samples originate from physically distinct devices, their inclusion significantly enhances the model's performance rather than degrading it. This suggests that the proposed UHDRL framework is robust to device

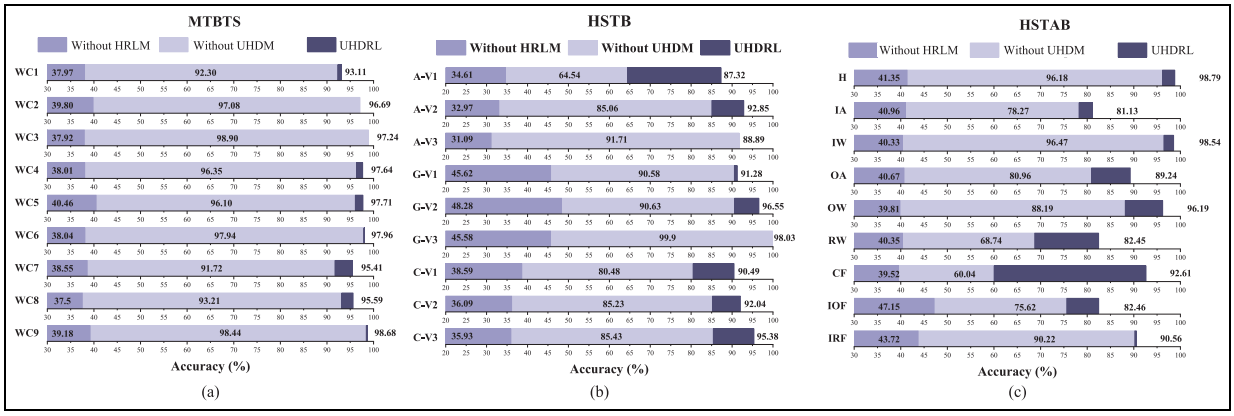

Figure 18. Impact of UHDM and HRLM on the proposed UHDRL (a) MTBTS (b) HSTB (c) High-speed train axlebox bearing.
UHDRL: Unified health domain relation learning; UHDM: Unified health domain mechanism; MTBTS: Metro train bogie transmission system; HSTB: High-speed train bogie; HRLM: Health relation learning mechanism.

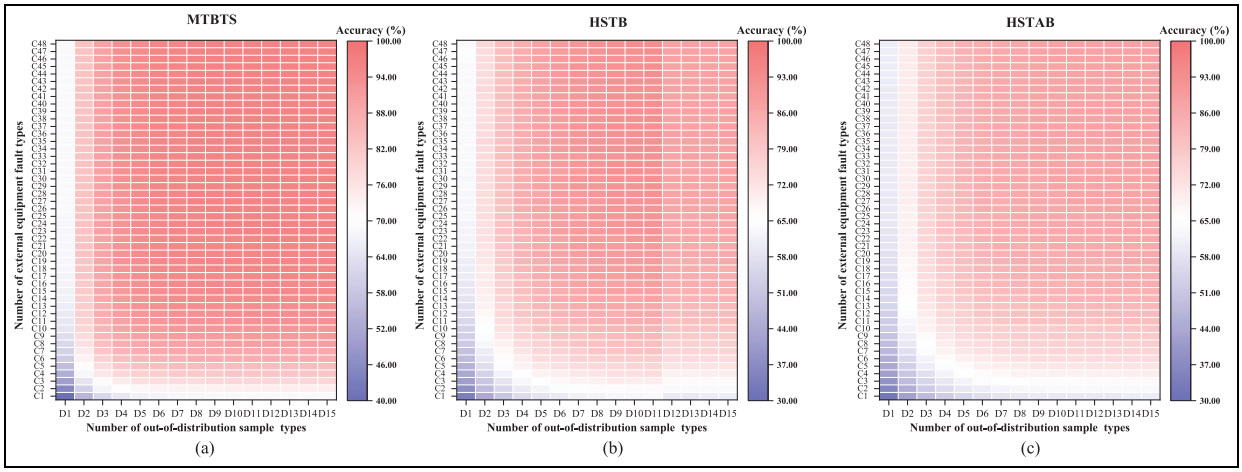

Figure 19. Effect of different PFSL category counts on UHDRL's fault detection performance (a) MTBTS (b) HSTB (c) High-speed train axlebox bearing.
UHDRL: Unified health domain relation learning; MTBTS: Metro train bogie transmission system; HSTB: High-speed train bogie; PFSL: Pseudo-fault sample library.

discrepancies. The external samples provide diverse "negative" constraints that force the model to learn a more compact and discriminative representation of the target device's health state. Specifically, the accuracy grows rapidly with the initial addition of PFSL types and stabilizes after reaching a certain threshold. This saturation indicates that the model has successfully captured the sufficient boundary information required to distinguish health states from anomalies. Consequently, while device differences exist, a comprehensive PFSL (when computational resources permit) is advisable, as it enriches the negative feature space and strengthens the decision boundary without being hindered by the domain shift of external data.

Comparison analysis. Representative DL and TL methods are selected for comparative analysis. For the DL methods, convolutional neural network (CNN) is employed, with training, validation, and testing datasets consistent with those used in the proposed UHDRL. For TL methods, domain-adversarial neural network[26] and deep subdomain adaptation network[30] are chosen, with the source domain consisting of health samples and PFSL, and the target domain consisting of health samples and fault state samples. Additionally, to broaden the comparison, classic fault detection algorithms such as convolutional auto-encoder (CAE)[31] and deep support vector data description (DSVDD)[32] are introduced. To ensure fairness in the comparison,

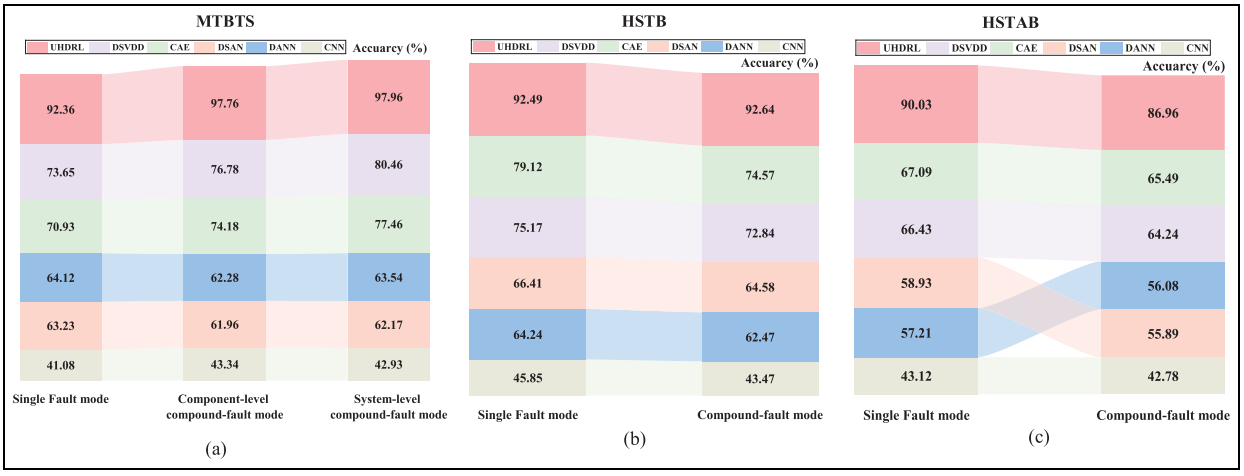

Figure 20. Analysis of the varying detection capabilities among different methods (a) MTBTS (b) HSTB (c) High-speed train axlebox bearing.
MTBTS: Metro train bogie transmission system; HSTB: High-speed train bogie.

the training parameters for all models, including learning rate, batch size, and optimizer settings, are consistent with those used in the proposed UHDRL.

Figure 20 presents the fault detection results across the two datasets. It is evident that the CNN model exhibits the poorest performance, with accuracy consistently remaining below 50%. This failure stems from the CNN's inability to generalize: trained exclusively on health data and the synthetic PFSL, the model overfits to the specific distribution of pseudo-faults and fails to recognize the distinct feature patterns of real-world anomalies. Conversely, TL approaches generally demonstrate better results, yet their accuracy typically stagnates below 70%. This performance bottleneck is primarily attributed to negative transfer: the significant distributional shift between the synthetic PFSL and actual physical faults, compounded by varying operating conditions, makes it challenging for TL models to align domains effectively without losing discriminative fault features.

The unsupervised methods, CAE and DSVDD, also exhibit relatively poor performance. These methods focus on mapping health samples to a latent space or hypersphere. However, due to varying operating conditions, the health data naturally forms a multimodal distribution (multiple scattered clusters). By failing to align these distinct operating modes, CAE and DSVDD serve to wrap a decision boundary around a dispersed data space. This results in an overly loose decision boundary that inadvertently encompasses fault samples, leading to low detection sensitivity.

In distinct contrast, the proposed UHDRL demonstrates superior performance, outperforming existing methods by a margin of more than 10%. By effectively mapping health states from diverse conditions into a unified, compact boundary space, UHDRL eliminates the intraclass variance that confuses other methods. This mechanism prevents the "loose boundary" problem of DSVDD/CAE and avoids the negative transfer issues of TL. These experimental results not only highlight the superiority of UHDRL but also validate its robustness and adaptability in handling complex, varying operating conditions.

Conclusion

This article proposes the UHDRL for fault detection in train transmission systems when fault samples are scarce and operating conditions vary widely. The framework combines a PFSL, a unified health domain mapping mechanism, and a health relation learning module to enrich training diversity with external pseudo faults, to align healthy-state representations across different operating conditions into a compact health manifold, and to strengthen discriminative power by learning relation scores between healthy and pseudo-fault features. The design intentionally avoids reliance on labeled fault data from the target domain to improve generalization to unseen fault conditions.

Extensive experiments on three testbeds under deterministic and nondeterministic operating regimes show robust quantitative performance. In the MTBTS the single-fault detection accuracy across nine operating conditions ranges from 86.91% to 97.41% and component-level and system-level compound-fault detection mostly exceed 90% with some evaluations averaging about 97.76%. In the HSTB, the average single-fault detection accuracy across tested conditions

exceeds 87% and gearbox detection peaks at 98.03% under the highest tested speed. In the HSTAB under nondeterministic conditions the average single-fault accuracy is approximately 90.03% and the average compound-fault accuracy is approximately 86.96%, while isolated low-performance cases occur, for example fault IA-1 with accuracy of 58.1% and a specific motor fault under one operating condition with accuracy near 27%. Comparative experiments indicate that UHDRL outperforms representative baselines by more than 10% points on average.

Ablation studies verify that both the unified health domain mapping mechanism and the health relation learning module are critical to overall performance, as removing either component leads to a clear degradation in detection accuracy, with more pronounced drops under nondeterministic operating conditions. The diversity of the PFSL shows a positive correlation with detection accuracy, with rapid improvements at early stages followed by saturation once sufficient negative coverage is achieved. From a practical perspective, UHDRL effectively reduces false alarms induced by operating-condition distribution shifts and exhibits strong performance in compound-fault scenarios, while challenges remain for extreme feature overlap and rare or subtle fault signatures. Trade-offs between pseudo-fault set size and computational cost are also evident, motivating future efforts toward adaptive pseudo-fault selection and augmentation, integration of few-shot or semisupervised learning strategies, lightweight online updating, and improved interpretability of relation scores for maintenance decision support.

Declaration of conflicting interests

The authors declared no potential conflicts of interest with respect to the research, authorship, and/or publication of this article.

Funding

The authors disclosed receipt of the following financial support for the research, authorship, and/or publication of this article: This research was partially funded by the National Natural Science Foundation of China (Grant No. 52405093), the Natural Science Foundation of Sichuan Province (Grant No. 2025ZNSFSC1269 and 2025ZNSFSC1325), and the China College Students' Innovative Entrepreneurial Training Plan Program at UESTC (Grant No. X202510614040).

ORCID iD

Zuoyi Chen https://orcid.org/0000-0001-7975-964X

Data availability statement

Data will be made available on request.*

References

1. Ding A, Qin Y, Wang B, et al. Evolvable graph neural network for system-level incremental fault diagnosis of train transmission systems. *Mech Syst Signal Pr* 2024; 210: 111175.
2. Song EZ, Zhu RJ, Yao C, et al. Generalized zero-shot bearing compound fault diagnosis based on reserved gate pre-classifier and physical information semantics. *Struct Health Monit*. Epub ahead of print 10 June 2025. DOI: 10.1177/14759217251338329.
3. Wang HB, Yan CF, Zhao YJ, et al. SEACKgram: a targeted method of optimal demodulation-band selection for compound faults diagnosis of rolling bearing. *Struct Health Monit* 2025; 24(1): 223–242.
4. Li Y, Meng XY, Xu FY, et al. Intelligent fault diagnosis of hoisting systems under complex working conditions using deep graph convolutional generative adversarial networks with limited data. *Struct Health Monit* 2025; 24(6): 3770–3791.
5. Ran GS, Li XY, Li M, et al. FD-Zero framework: LLM-based diagnosis framework for zero-shot mechanical time-domain signals. *Struct Health Monit*. Epub ahead of print 9 September 2025. DOI: 10.1177/14759217251366940.
6. Ye ZZ, Wu J, He XS, et al. Source-free domain adaptation framework for rotating machinery fault diagnosis by reliable self-learning and auxiliary contrastive learning. *Reliab Eng Syst Safe* 2025; 262: 111228.
7. Kumar A, Parkash C and Xiang JW. A robust entropy-based sparsity measure for health monitoring of rotating machinery. *Struct Health Monit*. Epub ahead of print 10 August 2025. DOI: 10.1177/14759217251346390.
8. Kumar A, Wylomanska A, Zimroz R, et al. Critical challenges and advances in vibration signal processing for non-stationary condition monitoring. *Adv Eng Inform* 2025; 65: 103290.
9. Zhao JY, He DQ, Jin ZZ, et al. A new method for bearing remaining useful life prediction based on dynamic wavelet and physical information constraints. *Expert Syst Appl* 2026; 296: 129023.
10. Chen ZY, Wu K, Wu J, et al. Residual shrinkage transformer relation network for intelligent fault detection of industrial robot with zero-fault samples. *Knowl Based Syst* 2023; 268: 110452.
11. Mao ZH, Wang H, Jiang B, et al. Graph convolutional neural network for intelligent fault diagnosis of machines via knowledge graph. *IEEE T Ind Inform* 2024; 20(5): 7862–7870.
12. Chen ZY, Huang HZ, Deng ZW, et al. Shrinkage mamba relation network with out-of-distribution data augmentation for rotating machinery fault detection and localization under zero-faulty data. *Mech Syst Signal Pr* 2025; 224: 112145.

13. Kumar A and Xiang JW. Robust adaptive ridge detection for frequency tracking in heavy-noise environment. *Adv Eng Inform* 2025; 68: 103774.
14. Zhang Q, Li SC, Chin-Hon T, et al. Fault impulse inference and cyclostationary approximation: a feature-interpretable intelligent fault detection method for few-shot unsupervised domain adaptation. *Reliab Eng Syst Safe* 2025; 253: 110568.
15. Wang H, Wang SH, Yang RG, et al. An optimized dynamic model improved deep discriminative transfer learning network for fault detection in rotation vector reducers. *Reliab Eng Syst Safe* 2024; 251: 110331.
16. Lu N, Hu HY, Yin T, et al. Transfer relation network for fault diagnosis of rotating machinery with small data. *IEEE T Cybernetics* 2022; 52(11): 11927–11941.
17. Luo JJ, Shao HD, Lin J, et al. Meta-learning with elastic prototypical network for fault transfer diagnosis of bearings under unstable speeds. *Reliab Eng Syst Safe* 2024; 245: 110001.
18. Chen XR, Li X, Yu SP, et al. Dynamic vision enabled contactless cross-domain machine fault diagnosis with neuromorphic computing. *IEEE -CAA J Automatic* 2024; 11(3): 788–790.
19. Zhang YC, Ding JL, Li YB, et al. Multi-modal data cross-domain fusion network for gearbox fault diagnosis under variable operating conditions. *Eng Appl Arti Intell* 2024; 133: 108236.
20. Guo L, Lei YG, Xing SB, et al. Deep convolutional transfer learning network: a new method for intelligent fault diagnosis of machines with unlabeled data. *IEEE Trans Ind Electron* 2019; 66(9): 7316–7325.
21. He C, Shi HM, Liu XR, et al. Interpretable physics-informed domain adaptation paradigm for cross-machine transfer diagnosis. *Knowl Based Syst* 2024; 288: 111499.
22. Sun SL, Wang TY, Yang HX, et al. An environmentally adaptive and contrastive representation learning method for condition monitoring of industrial assets. *IEEE T Cybernetics* 2024; 54(3): 1484–1496.
23. Zhou HX, Lei ZH, Zio E, et al. Conditional feature disentanglement learning for anomaly detection in machines operating under time-varying conditions. *Mech Syst Signal Pr* 2023; 191: 110139.
24. Hu CY, Wu JY, Sun C, et al. Mutual information-based feature disentangled network for anomaly detection under variable working conditions. *Mech Syst Signal Pr* 2023; 204: 110804.
25. Wu JY, Hu CY, Sun C, et al. Helicopter transmission system anomaly detection in variable flight regimes with decoupling variational autoencoder. *Aerosp Sci Technol* 2024; 144: 108764.
26. Ganin Y, Ustinova E, Ajakan H, et al. Domain-adversarial training of neural networks. *J Mach Learn Res* 2016; 17: 1–35.
27. Zhang XL, Wang YQ, Wei SQ, et al. Multi-scale deep residual shrinkage networks with a hybrid attention mechanism for rolling bearing fault diagnosis. *J Instrum* 2024; 19(5): P05015.
28. Hoffer E and Ailon N. Deep metric learning using triplet network. *Lect Notes Comput Sc* 2015; 9370: 84–92.
29. Lessmeier C, Kimotho JK, Zimmer D, et al. Condition monitoring of bearing damage in electromechanical drive systems by using motor current signals of electric motors: a benchmark data set for data-driven classification. *PHM Soc Euro Conf* 2016; 3: 1577.
30. Zhu YC, Zhuang FZ, Wang JD, et al. Deep subdomain adaptation network for image classification. *IEEE T Neur Net Lear* 2021; 32(4): 1713–1722.
31. Chen SM, Yu JB and Wang SJ. One-dimensional convolutional auto-encoder-based feature learning for fault diagnosis of multivariate processes. *J Process Contr* 2020; 87: 54–67.
32. Zhang Z and Deng XG. Anomaly detection using improved deep SVDD model with data structure preservation. *Pattern Recogn Lett* 2021; 148: 1–6.